The Meteoritical Society

Meteoritics & Planetary Science 1–21 (2020)
doi: 10.1111/maps.13592

The anatomy of fresh complex craters on the mid-sized icy moons of Saturn and self-secondary cratering at the rayed crater Inktomi (Rhea)

Paul SCHENK [1]*, Michelle KIRCHOFF [2], Trudi HOOGENBOOM[1,3], and Edgard RIVERA-VALENTÍN [1]

[1]Lunar and Planetary Institute, 3600 Bay Area Blvd, Houston, Texas 77058, USA
[2]Southwest Research Institute, 1050 Walnut Street, #300, Boulder, Colorado 80302, USA
[3]Seattle, Washington, USA
*Corresponding author. E-mail: schenk@lpi.usra.edu

(Received 04 September 2019; revision accepted 06 October 2020)

Abstract–Cassini mapping of Saturn's mid-sized icy moons of well-preserved complex craters in the 45–95 km size range provides insight into cratering processes at lower surface gravity and on icy targets. These craters are characterized by steep rim scarps, rugged hummocky floor deposits of curvilinear ridges and scarps, and rugged conical central peaks. Ponded impact melt or related deposits are not observed on any floor or ejecta units of any of these complex craters, indicating that melt production may be much lower than predicted. Mantling ejecta units drape over pre-existing topography, grading into concentric zones of secondary craters at ~1 crater diameter from the rim, demonstrating that secondaries occur on mid-sized icy planetary bodies. The largest and youngest bright-ray system is the 49 km central peak crater Inktomi, target of a mapping campaign down to 34 m pixel scales. In addition to classical secondary craters up to 3 km, several hundred small craters <1 km in size form an unusual densely spaced cluster across the eastern floor and ejecta deposit. The terrain-indiscriminate distribution of these eastern floor craters indicates they are not explosive volatile release pits, such as mapped on Vesta or Mars, but self-secondary craters formed by the fallback of ejected blocks back into the crater itself during crater formation. Self-secondaries likely formed by an irregular and stochastic but poorly understood impact process, such as spallation influenced by irregular surface topography. Self-secondary craters of this type could influence the interpretation of crater counts on large fresh impact craters and basins elsewhere.

INTRODUCTION

The mid-sized icy moons of Saturn (and Uranus and Pluto) provide an ideal natural laboratory for impact into objects with dominantly icy compositions in similar surface gravity regimes (g ~15–40 g cm^{-3}) intermediate between small irregular icy objects (g <10 g cm^{-3}) where strength begins to dominate and larger icy worlds such as Europa, Ganymede, and Titan (g ~120–140 g cm^{-3}). The well-established inverse gravity scaling of complex crater depths and the simple-to-complex transition diameters for icy satellites (Schenk et al. 2004; Schenk and Turtle 2009) has been most recently redefined for the Saturn system by White et al. (2013, 2017). Documenting the cratering process on these bodies adds to our general understanding of impact crater formation. Processes of interest here include collapse to produce complex crater landforms and ejecta formation, as observed by Cassini at high resolutions. A special emphasis of this work is the formation of ejecta deposits and secondary craters on these lower gravity worlds.

Secondary cratering has long been recognized as an important process in planetary cratering dating back to the acceptance of impact as the origin of lunar craters (Shoemaker 1967). Classical secondaries differ from primaries in their formation during discrete events associated with larger primaries and by their narrow size–frequency distribution, the peak of which is determined by the size and energy of the primary

cratering event. Thus, the study and comparison of ejecta and secondary crater formation on the mid-sized satellites of Saturn (and Uranus when data allow mapping of fresh crater morphologies) with those on larger icy objects such as Europa (Singer et al. 2013) and Ganymede (Hoogenboom et al. 2015) provide tests of impact formation models in icy surfaces.

The vast majority of secondary craters formed in a cratering event, which can number in the millions (McEwen et al. 2006), form in an annulus surrounding the primary source extending from circa one crater diameter from the rim and beyond (e.g., Gault et al. 1975; Schenk and Ridolfi 2002; Robbins and Hynek 2011). Terrains proximal to crater rims are normally (or assumed to be) crater-free immediately after impact due to the violent ballistic resurfacing that occurs within the thicker inner zone of the ejecta, though large deep highly mantled, pre-existing craters can often be identified within the ejecta deposit despite their obvious degradation. The radial transition from continuous ejecta to discrete secondary craters occurs as the volume of ejecta decreases radially from the rim. Dimensional scaling of this radial transition from continuous ejecta to discrete secondaries relative to crater diameter is theoretically scale independent (Housen et al. 1983; Housen and Holsapple 2011) and may be independent of target composition.

Recent mapping and studies of small craters superposed on large young craters on the Moon (Plescia and Robinson 2015; 2019; Zanetti et al. 2017), and mapping and simulations of distributed self-secondaries on slow-rotating bodies like Mercury (e.g., Xiao et al. 2016) and fast-rotating bodies such as Ceres (e.g., Neesemann et al. 2019) point to an increasing awareness that secondary craters can sometimes form within the ejecta deposit and perhaps even on the floors of the primary source crater itself (Shoemaker et al. 1968, 1969). These are referred to as "self-secondaries" (or "auto-secondaries") and may be an important and under-appreciated phenomenon in cratering (Xiao 2018) that could further contaminate primary cratering records and alter interpretations of the ages of young large craters (e.g., Hiesinger et al. 2012).

Secondary craters have relevance beyond impact mechanics. At present, both relative and absolute surface ages of bodies in the solar system beyond the Earth–Moon system can best be estimated from impact crater densities, a method dependent on an understanding of the projectile populations responsible for impact craters in these planetary systems (e.g., Zahnle et al. 2003). This process is especially difficult in the outer solar system, where extrapolation of lunar flux-based estimates is highly unlikely. The large numbers of widely dispersed secondaries from large primary craters can significantly influence the interpretation of crater counts and local age modeling of planetary surfaces (McEwen and Bierhaus 2006; Bierhaus et al. 2018). Cratering flux models in satellite systems of the giant planets are complicated by the potential for mixed populations (Kirchoff et al. 2018). Impact craters within satellite systems can be primary, secondary, or sesquinary (Bierhaus et al. 2018). Primary craters are made by direct impact of comets or, rarely, asteroids. Secondary craters are produced by impact of ejecta thrown some distance away by a primary impact and are more influenced by surface mechanical properties than their larger primaries. Sesquinary craters theoretically occur within a satellite system when debris escapes a satellite but returns later in widely scattered locations to create craters that might otherwise be interpreted as primary craters (e.g., Alvarellos et al. 2005). While we do not focus on this issue specifically, constraining these potential sources will better constrain the observed crater populations and derived ages within these planetary systems.

FRESH COMPLEX CRATER MORPHOLOGIES IN THE SATURN SYSTEM

Cassini global mapping of the five classical mid-sized icy moons of Saturn (excluding Enceladus where large pristine craters are rare) is essentially complete at pixel scales of ~200–400 m, depending on satellite (Schenk et al. 2018a). Concurrent imaging coverage in three colors in near-UV, green, and near-IR wavelengths (0.938, 0.556, 0.338 microns) provides global color mapping (e.g., Schenk et al. 2011). Stereo coverage is also essentially complete at similar scales. Higher resolution mosaics were acquired of selected regions covering 10–30% of satellite surfaces. Placements of many of these mosaics were dictated by encounter geometry, but some were targeted for tectonics or other major features. As a result, only a small number of large well-preserved impact craters in which original crater surface morphologies are preserved were observed at higher resolution.

The best resolved well-preserved complex impact craters observed by Cassini are Sagaris (diameter, D ~53 km; 5°N, 256°E) on Dione, Telemachus (D ~93 km; 54°N, 25°E) on Tethys, and Yu-ti (D ~67 km; 50°N, 278°E) on Rhea. Sagaris (Fig. 1) was observed in stereo at ~255 m pixel scales (orbits 221 and 222); Telemachus (Fig. 2) in stereo at 500 and 210 m pixel scales (Orbit 47); Yu-ti (Fig. S1 in supporting information) by Voyager at ~1 km pixel scales (VGR frame 34953.03) and then by Cassini in stereo and oblique imaging at 370–420 m pixel scales (CSS image number: N1710086684). Although these three craters have lost much of their bright ray patterns, they retain their

original floor and ejecta morphologies and are very well preserved (rim-to-floor depths are 4.5 km [Sagaris] and 5.8 km [Telemachus]). Floor materials have rugged hummocky textures characterized by tightly spaced curvilinear ridges, scarps, and mounds (Figs. 1 and 2). The steep rim scarps are usually abrupt single scarps with no indication of terrace formation, although large accumulations of ridged floor material are often observed at the base of these rim scarps. Rim crests are elevated a few hundred meters above the plains. The floor deposits are highest adjacent to the rim, suggesting they formed in association with rim failure, and converge in the center to form rugged but generally conical central peaks.

Sagaris formed on flat low-relief plains rather than rugged cratered highlands (Fig. 1), and as a result, a well-formed "pancake" or "abrupt termini" ejecta deposit (cf., Robbins et al. 2018) with a distinct outward-facing circumferential scarp is very evident (Figs. 1 and 3), as it is in a few other examples on Dione plains (e.g., Sabinus, D ~ 88 km; 44°S, 193°E). Similar scarp-bounded ejecta deposits 10s to a few hundred meters thick are common to Mars and to other low relief icy moons such as Charon (Robbins et al. 2018) and Europa, Ganymede, and Callisto (cf. Schenk et al. 2004). Telemachus formed on rugged cratered uplands (Fig. 2), and while a mantling ejecta deposit is also present, the scarp-defined ejecta margin is not evident, presumably because the rugged pre-existing topography makes such a subtle feature difficult to form or detect due to rapidly changing slopes. No ponded flat-lying impact melt deposits are resolved at any of the craters studied in this size range, although very minor melt-related features <0.5 km across could be below the limit of resolution.

Evident at both Sagaris and Telemachus (Figs. 1–3) is the transition from the scoured ejecta-mantled topography surrounding these craters to the extended fields of small noncircular craters and irregular crater chains at ~1 crater diameter from the respective rims. These small irregular craters at these sites are absent in the mantled ejecta zone but are mixed into and can be difficult to distinguish from the small primary cratering record in the region, especially in the absence of associated bright ray albedo patterns. The most easily recognized secondaries (by virtue of their irregular shapes, irregular chains, and proximity) are typically 1–1.5 km in diameter at Sagaris and 2–3 km at Telemachus, broadly consistent with expected largest secondary crater diameters based on the ~0.04 $D_{\text{secondary}}/D_{\text{primary}}$ ratio rule on the Moon (Allen 1979) and 0.04–0.05 for larger icy satellites (Singer et al. 2013) although we have likely not yet identified the largest secondaries from these craters.

Yu-ti (D ~ 67 km) on Rhea (Fig. S1) also formed in rugged highlands and, although not as well observed as

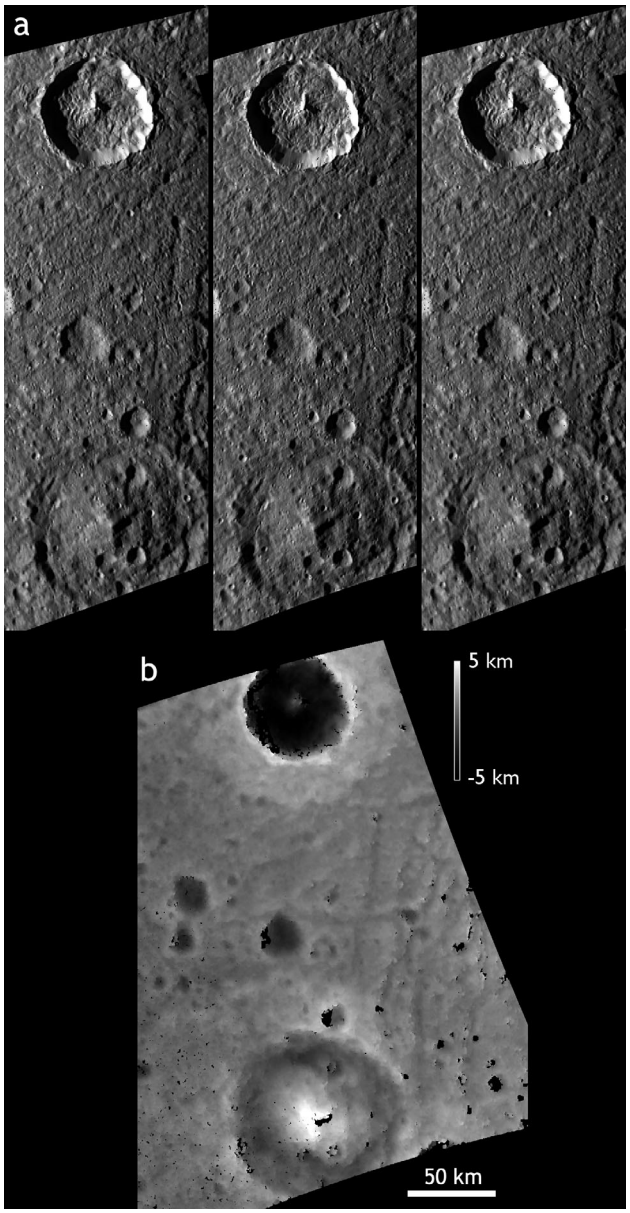

Fig. 1. a) Cassini stereo images of well-preserved 53 km wide Dione central peak crater Sagaris (5°N, 256°E; top). Cassini orbit 139 images at ~190 m pixel scale. Note viscously relaxed degraded 77 km crater Lagus (bottom) with prominent central peak. Figure format allows user to view in either wall-eyed mode (left-center) or cross-eyed mode (center-right). North is toward top. Slight Sun shift between exposures causes shadow distortions. Cassini image numbers N1665974861.096 and N1665972106.088. b) Digital elevation models (DEM) of 53 km wide Sagaris (near top), corresponding to area of Fig. 1a. Note elevated annular plateau flanking Sagaris rim, relaxed crater Lagus with prominent central peak at bottom center (White et al. 2017), and shallow fractures in right side of map. Vertical scale bar shows elevation range displayed. Except where noted, all DEMs shown are produced from stereogrammetry using the methods of Schenk et al. (2018b) and have vertical precisions of ~35–50 m. DEM dropouts are due to shadows.

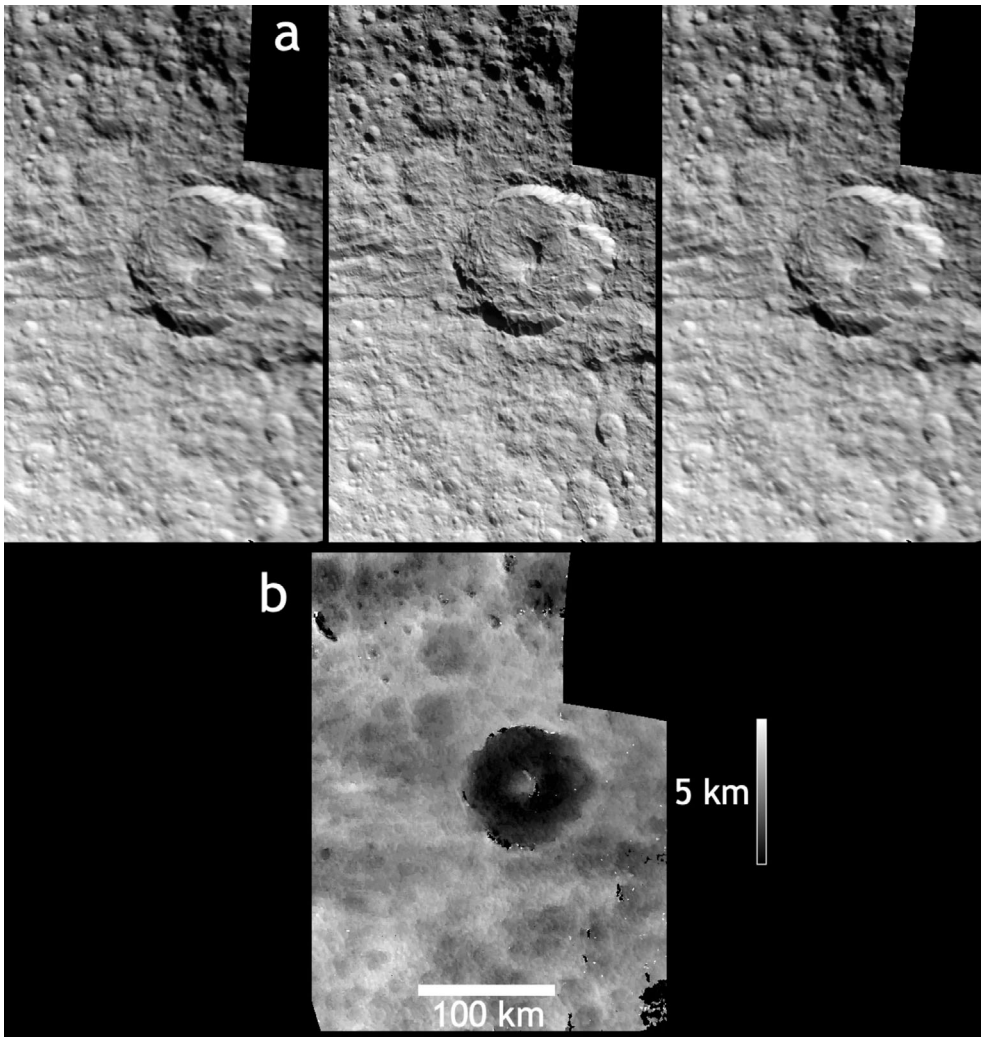

Fig. 2. a) Cassini stereo pair of 93 km wide central peak crater Telemachus (54°SN, 25°E) on Tethys. Cassini orbit 49 images acquired at ~500 m (left and right) and 220 m (center) pixel scales. Horizontal striations are part of the older Ithaca Chasma trough system. Figure format allows user to view in either wall-eyed mode (left-center) or cross-eyed mode (center-right). North is toward right. Cassini image numbers N1561669628.103 and N1561674168.103. b) DEM elevation map of 93 km wide Telemachus crater Tethys. See (a) for spatial orientation. Vertical scale bar shows elevation range displayed.

Saginus and Telemachus, mantling ejecta and irregular kilometer-wide craters and chains are evident at similar scaled distances from the rim (Schenk and Ridolfi 2002). Deceleration ridges may be evident in the ejecta here (and at other sites; e.g., Figs. 3 and 14) where ballistic material was impeded by topographic scarps, as well as at least one apparent landslide at the base of the rim scarp. Deceleration dunes may be evident on the rim flank of a well-preserved 9 km bright ray crater on Dione (Fig. S2 in supporting information).

The largest rayed crater on Dione is 34 km wide Creusa (49°N, 284°E; Fig. S2), best observed in orbit 222 at ~270 m pixel scales in stereo and in color. The stereo views reveal that Creusa has a single steep rim scarp and hummocky floor with curvilinear ridges and scarps rising to a small central peak, essentially a smaller version of Telemachus and Sagaris. The images reveal a mantling ejecta deposit around Creusa but are insufficient to confidently distinguish secondaries from small primaries, though there is some uncertainty as to whether Creusa would be large enough to produce them (Bierhaus et al. 2012). The ray pattern at Creusa is also very extensive, extending over almost an entire hemisphere (Hirata and Miyamoto 2016).

The floor and ejecta morphologies observed at Sagaris and Telemachus are very typical of younger complex craters in the 10–125 km size range on these satellites (Figs. 1–3; Figs. S1 and S2), though secondary craters are not recognizable for any other craters due to

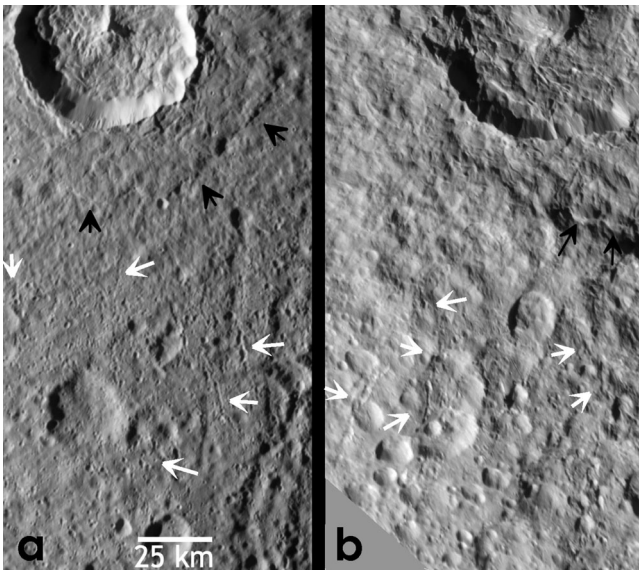

Fig. 3. Enlargements of Figs. 1a and 2a highlighting small fresh-looking secondary craters and elongate crater chains (white arrows) at Sagaris (a) and Telemachus (b) craters (at top). Note the paucity of these small craters and chains in the zone flanking the crater rims. Black arrows highlight rampart scarp at edge of thicker ejecta and (at right) possible deceleration ridges at base of local scarp.

resolution and degradation issues. We note that the more subtle floor ridge structures and shallower secondary craters tend to be among the first crater features degraded and ultimately erased by erosive processes. High solar illumination can also make such features difficult to recognize.

Inktomi Crater (Rhea)

Early Cassini images of Rhea revealed a prominent bright ray system centered on the fresh 49 km wide complex crater Inktomi at 14°S, 248°E (Fig. 4; Fig. S3 in supporting information), the most prominent ray pattern and likely youngest large crater in the Saturn system. As a result, Cassini targeted Inktomi twice for high-resolution observations (Table 1). A single wide angle (WA) ISS image of the eastern rim and proximal ejecta deposit was acquired at 34 m pixel scales in orbit 18 (Fig. 5), with one narrow angle (NA) image at 6 m pixel scales nested at the center of the WA image. This was supplemented by a single NA frame at 6 m pixel scales within the bright ray pattern west of the rim (Fig. 6). This was followed by high-resolution ISS and VIMS imaging sequences over Inktomi in orbit 49 (Fig. 7), highlighted by two stereo images of the crater rim and floor acquired at 35 m pixel scales (Fig. 8). These observations were followed by a 12-frame mosaic of all of Inktomi and its continuous ejecta deposit and

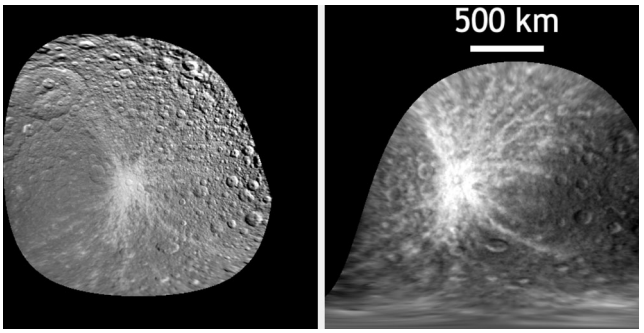

Fig. 4. Two low-resolution views of Rhea showing the extent of the Inktomi bright ray system under different illumination conditions. These images from orbits 21 (left) and 10 (right) are shown in cylindrical map projection at 2.0 and 6.6 km/pixel and extend from −90° to +90° latitude and ~200° to 300° E longitude. The view at right was acquired under higher solar illumination. Figure S3 is a higher resolution view of the central portions of the ray system. Cassini image numbers N1519487727.110 and N1498350342.076.

parts of the ray pattern at pixel scales ranging from 40 to 90 m, supplemented by three contemporaneous mosaics in near-UV, green, and near-IR wavelengths in 2x2 pixel summation mode (Fig. 7), and by an oblique color sequence at ~490 m pixel scales of the crater and inner ray pattern on departure from Rhea (Fig. 8).

These observations give us an exceptional view of the crater floor and the entire ejecta deposit and inner sections of the secondary cratering field, as well as the extended secondary and ray patterns ~5 crater radii to the west. The orbit 18 and 49 observations provide several stereo combinations which have been used to produce stereo pairs for geologic interpretation of most of the crater floor and the influence of topography of ejecta and secondary crater formation and for production of digital elevation models (DEMs). Later imaging in orbit 162 (Table 1) also provides low-Sun morphologic context views at ~250 m pixel scales (Fig. S4 in supporting information), which is particularly relevant to the Dione and Tethys examples in Figs. 1 and 2 as it shows the same pattern of distrusted small fresh crater outside the continuous ejecta zone of Inktomi as we document at those craters.

The extensive bright rays of Inktomi radiate up to ~900 km from crater center, and thus extend over most of the Inktomi-centered hemisphere (Fig. 4). Long bright rays may extend 1500 km onto the trailing hemisphere in the form of two arcuate bright streaks that appear to radiate from the eastern ray pattern (e.g., ISS frame W1646249633.118), and were observed by Voyager (Fig. S5 in supporting information). The ray pattern is asymmetric (Fig. 4), with the longest rays extending north and south and the shortest rays in the western sectors, suggesting an oblique impact from that

Table 1. Principal Cassini images of Inktomi crater used in this investigation.

Orbit	Image number	Resolution (m/pxl)	Phase angle	Color filter	Crater counting site[a]
18	N1511700242.121	1755	19	UV3	
18	N1511700272.121	1755	19	Green	
18	N1511700332.121	1755	19	IR3	
18	N1511737558.116	7	95	Clear	WestVHR
18	W1511737577.116	6.5	95	Clear	East Rim
18	N1511737577.118	33	95	Clear	East Rim
49	N1567130234.122	35	38	Clear	
49	N1567130338.120	37	30	Clear	East Floor
49	N1567130480.120	38	25	Clear	
	through	-	-	IR3/G/UV3	West Ejecta
49	N1567132001.120	87	27		
49	W1567131212.118	567	18	Clear	
49	N1567132450.118	103	31	Clear	
49	N1567132483.118	206	31	UV3	
49	N1567132500.118	206	31	Green	
49	N1567132517.118	206	31	IR1	
49	N1567132534.118	206	31	IR3	
49	N1567138507.118	680	43	UV3	
49	N1567138524.118	680	43	Green	
49	N1567138541.118	680	43	IR1	
49	N1567138558.118	339	43	Clear	
49	N1567141926.118	478	44	Clear	
49	N1567142176.118	956	44	UV3	
49	N1567142209.118	956	44	Green	
49	N1567142242.118	956	45	IR1	
49	N1567142275.118	956	45	IR3	
162	N1710087543.120	260	59	Clear	

[a]See Fig. 16.

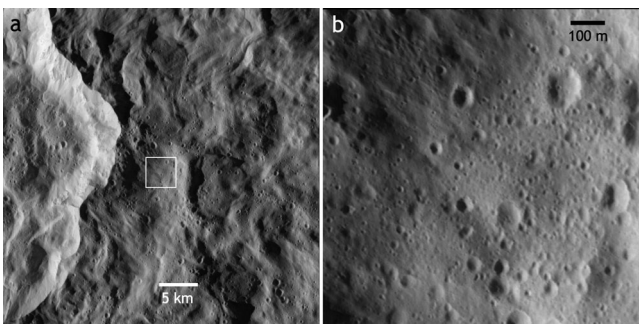

Fig. 5. Cassini orbit 18 WA (a) and NA (b) images of eastern rim scarp and ejecta deposit of Inktomi crater. Views were acquired at scales of ~32.6 and ~6.5 m/pixel, respectively, among the highest resolution views of Rhea. Square shows location of NA frame within WA image. Note transition from nearly crater-free surface at top of WA view to densely cratered surfaces in most of the remaining areas. This site is referred to in our crater counting as "East Rim." Cassini image numbers W1511737577.116 and N1511737577.118.

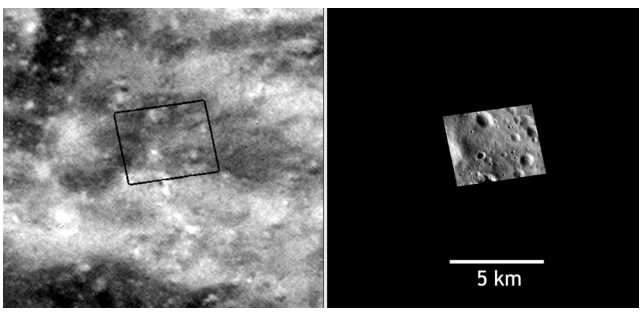

Fig. 6. Cassini views of bright ray patterns due west of Inktomi crater rim. Left) Context image from orbit 49 acquired at ~50 m/pixel showing area ~17 km wide; (right) NA orbit 18 image in same map projection at 7.3 m/pixel. The high-resolution image lies between two east–west branches of the bright ray system (at lower center and upper left center of left image) and except for one bright crater likely reveals ordinary background cratering at very high resolution. This site is referred to in our crater counting as "West VHR." Cassini image number N1511737558.116 (at right).

direction (Wagner et al. 2008). Some rays also appear to deviate slightly from true radial orientation, possibly related to satellite rotation during emplacement. Although we suspect that the specific directions of the most prominent rays could be related to rugged crater-dominated topography of the pre-existing surface and/or planetary rotation, a detailed three-dimensional impact simulation would be required to test this.

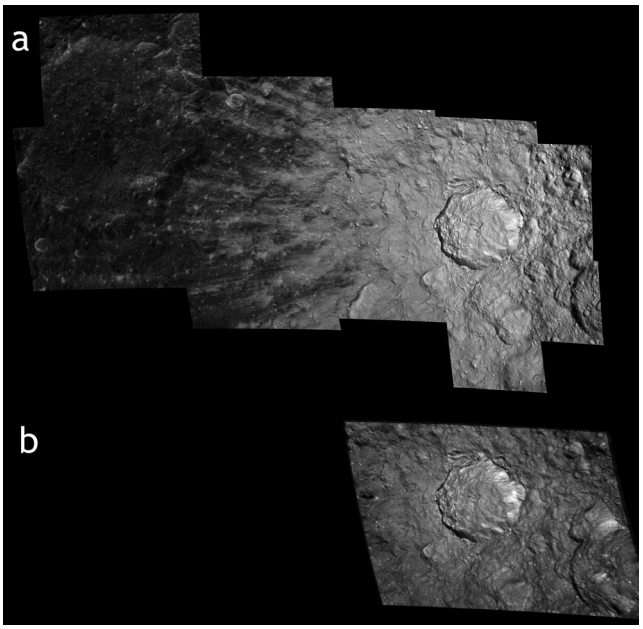

Fig. 7. Cassini orbit 49 targeted color observations of 49 km wide bright ray crater Inktomi, Rhea, projected to same orthographic map projection centered on the crater. (a) Fifteen-frame NA four-color mosaic at 40–95 m pixel scales. (b) Oblique NA three-color image set acquired at ~210 m/pixel. Additional orbit 49 images are highlighted in succeeding figures. Color versions and additional images from these sequences are provided in the supporting information.

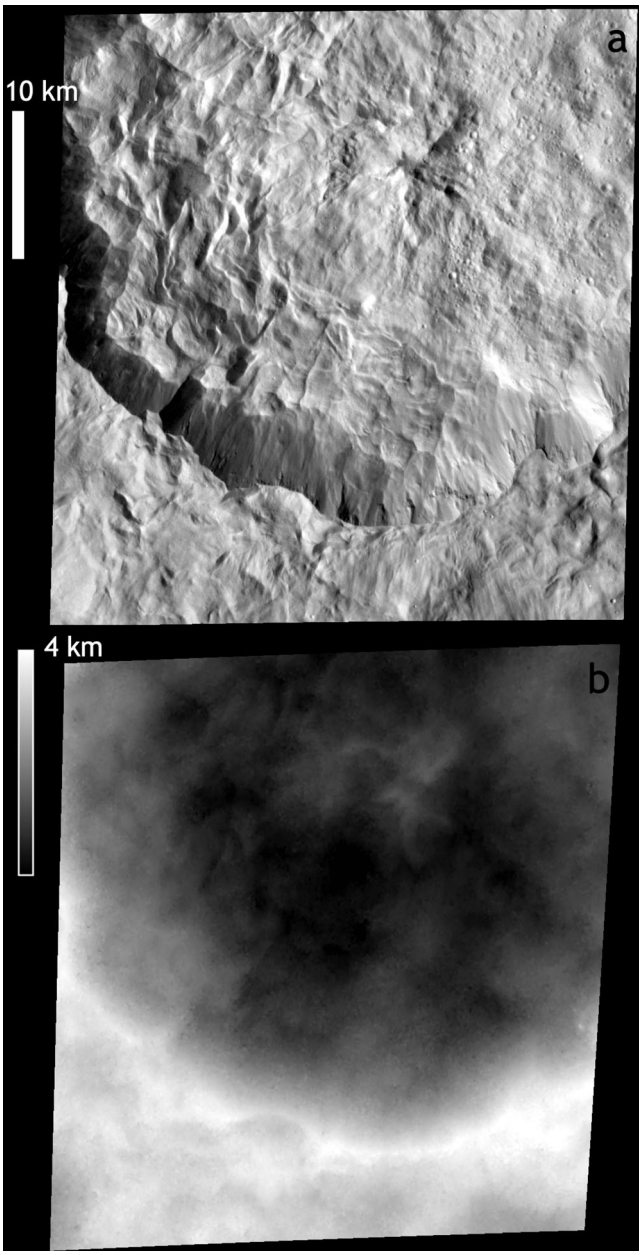

Fig. 8. a) High-resolution image of most of Inktomi rim and floor, acquired in orbit 49 at pixel scales of ~35 m. A second frame acquired consecutively provides stereo (Fig. 9b). Note abundant small craters on eastern floor, the site referred to in our crater counting as "East Floor." Cassini image number N1567130234.122. North is to top. b) Stereogrammetric DEM of floor and rim of Inktomi, based on stereo data shown in Figs. 8a and 9. Vertical scale shows 4 km of relief. Colorized version in supporting information.

Morphology

The interior morphologies of Inktomi (Figs. 8 and 9) are very similar to those observed at Sagaris, Telemachus, and others (Figs. 1–3; Figs. S1 and S2). The rim crest of Inktomi forms a mostly continuous steep inward-facing scarp of variable height (Figs. 8 and 9) but averaging ~3 km with maximum slopes of 35°–40°. Beginning at the base of this scarp, hummocky floor materials characterized by sinuous rolling ridges, scarps, and mounds form an "interwoven" pattern (Figs. 8 and 9). Some of the thickest and highest standing debris mounds are associated with reentrant alcoves along the rim wall scarp, indicating enhanced rim wall failure in those locations. The crater floor has a double catenary profile centered on the central peak (Figs. 8, 9, and 11). Two breaks in slope occur where the rim scarp transitions to accumulated floor material debris at the base of the rim scarp and then again when these transition to flatter floor materials before rising to form the central peak. The mean depth of Inktomi is ~3.6 km (as measured from the rim crest to the deepest part of the floor proximal to it), but this depth is also variable to ±0.5 km along the circumference.

The floor ridges and scarps grade into a central peak complex ~14 km wide and ~1.25 km high above the uneven floor (Figs. 8 and 11). The central peak is less a simple cone as it is in some other Saturnian craters, but rather a complex arrangement of converging ridges and massifs of various heights, forming a broadly conical-shaped massif (Figs. 8, 11; Fig. S7 in supporting

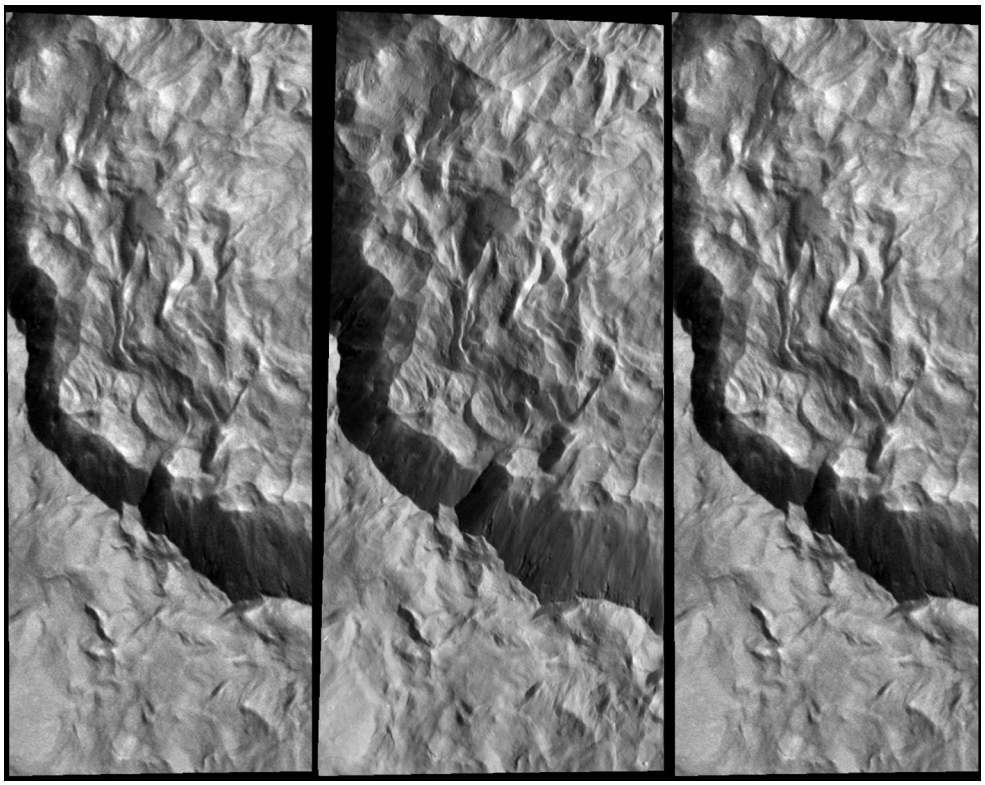

Fig. 9. Stereo view of western floor and rim of Inktomi crater, using image data in Fig. 9. Figure format allows user to view in either wall-eyed mode (left-center) or cross-eyed mode (center-right). Rugged ejecta relief, steep rim scarp, and floor scarps and ridges are evident. Effective pixel scale of 35 m. The base of the central peak is at top right. Cassini image numbers N1567130234.122 and N1567130388.120.

information). Several small discrete debris slides 1–2 km wide and 20–50 m high are evident along the base of the rim scarp, especially along the northeastern rim wall (Fig. 10; Fig. S6 in supporting information), but these post-date and are volumetrically insignificant compared to the extensive debris mounds and ridged units covering the crater floor.

Sculpted ejecta deposits surround Inktomi to a mean distance of ~43 km from the rim scarp (Figs. 8 and 12) and mantle rugged pre-existing topography of 1–2 km. Most of this topography is due to older craters of different sizes and ages, some of which are evident in the stereo views. Surface striations indicative of lateral flow and accumulation of ejecta material are evident across much of the deposit (Figs. 8 and 12), including at the bases of pre-existing crater walls. As at Sagaris and Telemachus (Figs. 1 and 2), no evidence for ponded flat-lying deposits typical of refrozen impact melt in large lunar, mercurian (e.g., Chapman et al. 2018), Martian (e.g., Mouginis-Mark and Boyce 2012), and even larger cerean (e.g., Schenk et al. 2019) impact craters with significant volumes of impact melt is observed on the ejecta or floor deposits of Inktomi (Fig. 9). Narrower leveed melt flows of the type observed on the Moon (Kruger et al. 2016) are also not observed at Inktomi, but whether this is due to absence or inadequate resolution is not known. Although some smaller features might be unresolved, we conclude that despite a thick mantling ejecta deposit, impact melt production at Inktomi was likely very limited, negligible, or not preserved on the surface (see the Discussion section).

The apparent outer margin of this mantling ejecta deposit (as determined by obscuration of small craters and textural changes) is variable in distance from the rim, ranging from ~33 km to ~57 km. These variations likely reflect the influence of the rugged pre-existing topography in both the ejection and deposition processes. Despite this variability, the average lateral width of this mantled ejecta zone of ~0.9 crater diameter from the rim is very similar to that observed at Sagaris and Telemachus (Figs. 1–3). It is also broadly consistent with observed ejecta deposit widths as measured on the Moon and other icy bodies, including Ganymede and Europa (Schenk and Ridolfi 2002; Bierhaus et al. 2012). It should be noted these are measured relative to the observed rim scarp, which has been widened by rim failure from the original

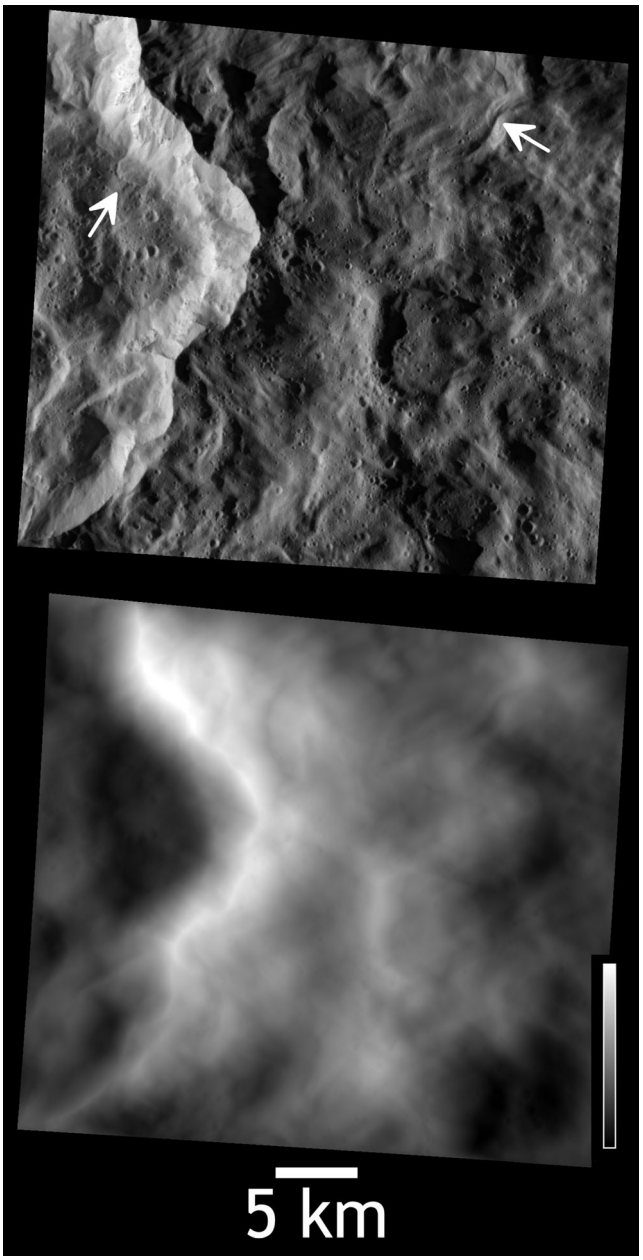

Fig. 10. Image and stereo-photoclinometric DEM of eastern rim and ejecta units of Inktomi. Note small lobate landslides at base of northeastern rim scarp (left arrow) and possible deceleration ridge adjacent to scarp (right arrow). Image and Dem at 32 m pixel scales; north is to top; vertical scale shown is 3.5 km.

excavation cavity, and that this widening process may not be equally efficient on all planetary bodies.

The entire crater, but especially the rim wall and central peak, features the strongest water ice absorption bands on Rhea (Stephan et al. 2012). These are the purest water ice exposures on the surface (Stephan et al. 2012) and presumably represent areas of ice uplifted or exposed from below the optical surface or the shallow regolith during impact, relatively uncontaminated by ongoing deposition of magnetospheric and meteoritic grains.

The Inktomi ray system is essentially neutral in IR/UV and Green/UV ratio images and only moderately dark in IR/Green ratios (Fig. S8 in supporting information) indicating a slight blueness due to a weaker signature in the near-IR. This signature appears to increase to some degree as phase angle increases in color imaging, suggesting a phase angle dependence worth further investigation. The UV-Green-NIR color ISS images also reveal that most of the rim wall and parts of the central peak of Inktomi are UV-bright, giving them a bluish color in the three-color renditions (Figs. S4 and S8). This coloration is similar to that observed on rim wall scarps and other steep slopes on Rhea that are not ancient (Fig. S8), as well as the equatorial Blue Pearls that are attributed to reimpact of ring particles onto the surface at local promontories (e.g., Schenk et al. 2011). This bluish coloration is often ascribed to the exposure of larger ice grains (or perhaps purer water ice grains) from deeper levels within the rim wall scarp, or to downslope creep and exposure of icy materials that have not been contaminated by magnetospheric implantation or E-ring deposition (e.g., Schenk et al. 2011), consistent with the VIMS spectroscopic interpretation (Stephan et al. 2012).

Age of Inktomi. Voyager did not observe Inktomi favorably in any of its 1980–1981 observations, but examination of the low-phase-angle mosaic of the leading hemisphere of Rhea obtained at ~1 km pixel scales shows bright patches that correspond with distal eastern rays from Inktomi mapped later by Cassini (Fig. S5). These confirm that Inktomi formation must predate 1980. Wagner et al. (2008) estimated an age of 250 to 8 Ma, depending on assumed flux. Randomly scattered and hence postimpact craters on the mantling ejecta deposit are very rare but can be identified (Fig. 11), all smaller than 0.5 km in size. Excluding the heavily cratered eastern quadrant (see below), the spatial densities of these widely scattered small primaries >200 m in diameter (the effective detection limit) are extremely low (Fig. 12), ~1 crater per 100 km^2. Assuming these are post-Inktomi primary craters and avoiding the pitted floor and easternmost ejecta, we estimate a formation age of Inktomi of circa 10 Ma, assuming a projectile population dominated by Kuiper Belt and/or Jupiter-family comet objects (e.g., Zahnle et al. 2003). Such estimates are useful only as far as the assumptions are valid, as crater counts in small areas of low crater density are often unreliable due to stochastic variability and locally variable secondary contamination (e.g., Williams et al. 2018). If some of these rare widely scattered post-Inktomi craters used here are also due to

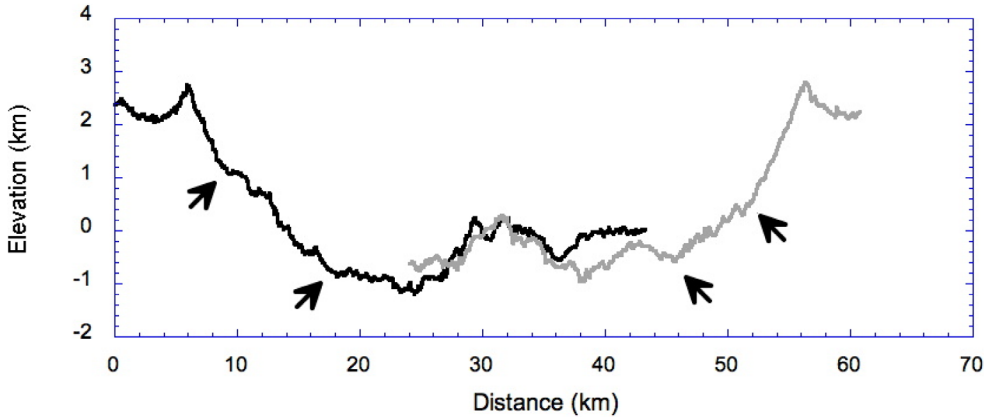

Fig. 11. Two representative topographic profiles from stereogrammetric DEM of floor and rim of Inktomi crater. Arrows highlight breaks in slope from rim scarp (top section) to hummocky rim debris to hummocky floor deposits (bottom sections). The two profiles do not spatially overlap and show natural variations in topography of the crater floor.

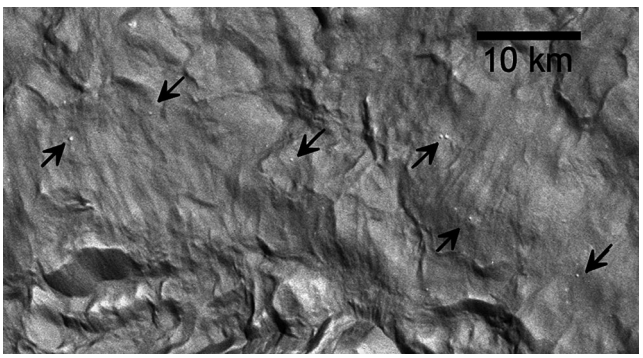

Fig. 12. Views of postimpact craters (arrows) within ejecta units at Inktomi. Rim scarp is visible at bottom.

sesquinary impacts derived from Inktomi itself, then the age of Inktomi would be even younger.

Secondary Craters at Inktomi

External to the mantling ejecta deposits at Inktomi in all quadrants, we observed fields of smaller craters up to a few kilometers in size (Figs. 6, 13; Fig. S9 in supporting information). These craters are distinct from ordinary randomly distributed and typically circular background craters by virtue of their pristine (i.e., unmantled by ejecta) rim morphologies, distinctly irregular noncircular shapes, high apparent brightness (comparable to Inktomi and its ejecta, most being spatially associated with the bright rays of Inktomi), and by variable degrees of clustering. These are all features characteristic of secondary craters in a manner consistent with those observed on other planetary bodies. One narrow relatively pristine crater chain or groove ~10 km long within these crater fields is oriented radially to the northern rim (Fig. 13; Fig. S9), and likely a secondary crater chain of the type also observed on other planets. Though also variable, the inner boundary of this concentric crater zone lies on average ~0.9 crater diameter from the rim, with the inner limit of this zone corresponding reasonably closely with our mappable limits of continuous ejecta (e.g., Schenk and Ridolfi 2002; Robbins and Hynek 2011).

Interior Craters at Inktomi—The Eastern Quadrant

Despite the extreme paucity of superposed craters and very young inferred age of Inktomi (Fig. 12), hundreds of small craters all <1 km in size are concentrated across the eastern part of the crater (Fig. 14). These craters form a relatively well-delineated and mappable grouping or field (Fig. 15) in a crude east–west-oriented oval ~50 by 20 km in size centered on the eastern rim scarp and overlapping the eastern half of the central peak, eastern floor quadrant, and proximal eastern ejecta deposit. These craters are densely spaced on the crater floor but less so as one goes from west to east. The small craters formed within the rugged mantled eastern ejecta units with ~1 km of relief (Fig. 14c) typical of the densely cratered terrains that constitute most of Rhea's surface. This elliptical zone of densely concentrated small craters within and proximal to the rim of Inktomi, and well interior to the concentric zone of classical secondaries (Fig. 15), is highly unusual for a large impact crater of any age on any planet.

Secondary Crater Populations in the Saturn System: Inktomi

To characterize the populations of secondaries and fragment sizes of postimpact fragments on mid-sized icy

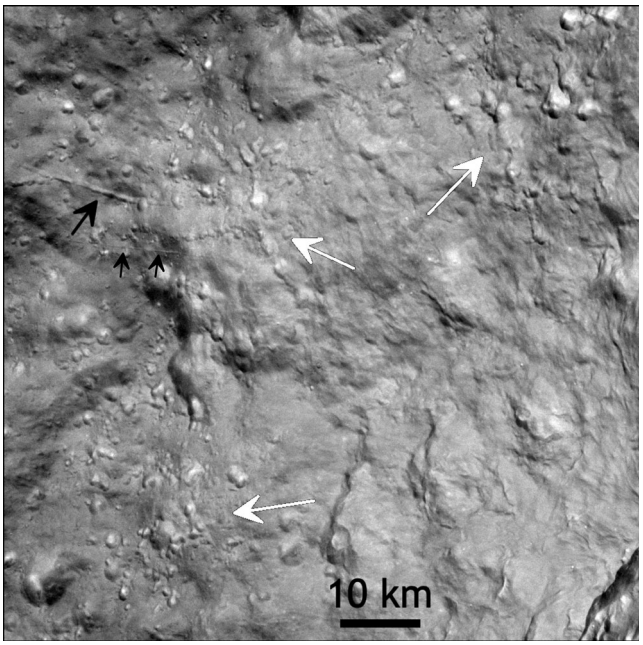

Fig. 13. View of northern and western continuous ejecta and secondary crater field of Inktomi crater. Irregularly shaped and sharp-rimed secondary craters are prominent at center left and upper right. Also visible at upper left is a linear crater chain apparently originating from Inktomi, the rim of which is just visible at bottom right. The area at lower left is the counting area referred to in our crater counting as "West Ejecta." Muted circular depressions in areas proximal to the rim are older craters buried beneath the extensive mantling and striated ejecta unit. Cassini image number N1567131 452.118.

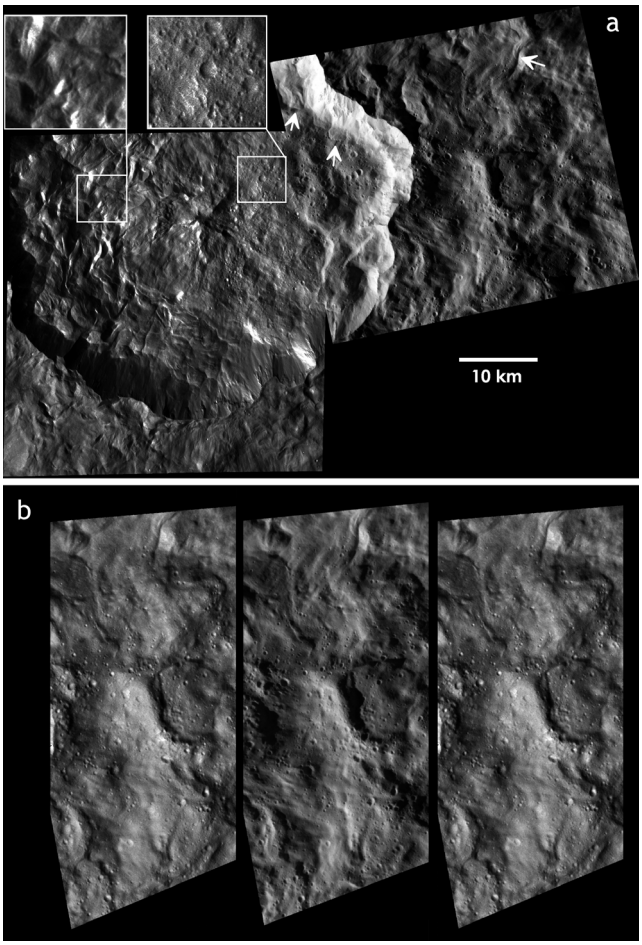

Fig. 14. a) Mosaic of highest resolution orbit 18 and 49 images of Inktomi floor and eastern ejecta deposit. Images were acquired at pixel scales of 32–37 m. Insets show the two areas marked by white boxes, highlighting the lack of craters on the western floor and dense craters on the eastern crater floor deposits. Arrows point to landslides on northeast rim and deceleration ridges in the ejecta deposits. Mosaic of Cassini image numbers N1567130388.120 and N1511737577.116. b) Stereo view of eastern ejecta deposit of Inktomi crater, combining orbit 18 WA image and orbit 49 NA image from four-color mosaic. Crater rim is just out of view at center right. Figure format allows user to view in either wall-eyed mode (left-center) or cross-eyed mode (center-right). Shadows shifted slighted between exposures. Note the absence of smooth flat-lying materials in topographic lows. Cassini image numbers N1511737577.116 and N1567130 633.100.

satellites, we measure craters at several sites associated with Inktomi (Figs. S10 and S11 in supporting information; Table 1), including the proximal western classical secondary cratering field (West Rim; which has the most contiguous image coverage), craters on Inktomi floor (East Floor), and craters on the eastern rim (East Rim; at two resolutions). To characterize populations nominally uncontaminated by Inktomi secondaries (based on a lack of bright ray material), we examine a medium resolution site for cratered terrains far from Inktomi (Fig. S12 in supporting information). We also examine a serendipitous site using the one high-resolution observation located between two bright rays (Fig. 6), which includes background cratering near Inktomi. The high-resolution imaging allowed craters down to 150 m to be resolved. The zone of secondaries that can be reasonably identified from background small cratering is limited at Inktomi to the zone between 1 and ~2 crater diameters from the rim. This is mostly due to the complex ray brightness patterns and the normal background cratering (Fig. 7) in areas farther out from crater center. Older degraded craters without the defining characteristics of secondaries in the western secondary counting area were excluded from the counts as our interest was in defining the SFD of the secondaries. While all the authors reexamined the counts and edited them to produce final consensus counts, it is possible that a small percentage of our secondary counts are small primary or even sesquinary craters.

Crater counts in both the western secondary and the eastern floor/ejecta crater fields at Inktomi

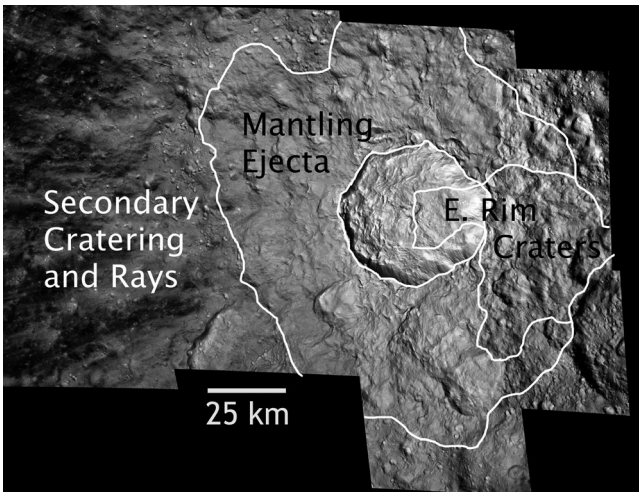

Fig. 15. Sketch map of Inktomi crater and inner ray system, highlighting major units, including the crater floor (unlabeled), the mantling ejecta unit, secondary cratering field (and inner ray system), and the eastern rim and floor crater field

(Figs. 13, 16; Figs. S10–S12) show that craters in both areas have a size–frequency distribution (SFD) different from our reference heavily cratered areas, which have SFDs comparable to those representative of Rhea on a larger scale (Kirchoff and Schenk 2010). On an R-plot, the "classical" secondary craters observed in the western sector of the secondary field (Figs. 13 and 16) peak in relative density at around ~1–2 km, approximately twice those of the craters in the eastern Inktomi floor cluster. The spatial density of craters within the eastern floor/ejecta field peak at a diameter of ~100–400 m, with those on Inktomi floor being almost a factor 2 larger than those on the rim flank, which may correlate with the higher spatial density of such craters, indicating that the crater field is asymmetric. We note, however, that while the largest diameters are very well defined, the smallest diameter craters are likely unresolved or have low confidence and the smaller crater statistics may be incomplete. All data are plotted only for craters larger than ~5 times the pixel scale of the associated imaging.

At ~2.2 km, the largest confidently identified secondary crater in the western secondary crater counting area (Figs. 12, 15; Fig. S10) is ~$0.044D_{\text{inktomi}}$. The largest likely secondary crater in the entire orbit 49 mosaic (Fig. 15) is ~3 km, giving a secondary/primary diameter ratio of ~$0.06D_{\text{inktomi}}$, proportionately larger than known secondary craters on the Moon (Allen 1979) and slightly larger than on Europa (Singer et al. 2013) and Mars (Robbins and Hynek 2011) relative to their primaries. While these values are consistent with secondary crater size ranges generally, greater degrees of rim failure on the Moon would increase the apparent primary diameter and decrease the measured $D_{\text{secondary}}/D_{\text{primary}}$ ratio and could explain larger apparent secondaries on icy bodies (Singer et al. 2013; this report). Comparing secondary sizes to transient crater diameters might result in more similar diameter ratios.

Fragment sizes for the largest classical secondary craters (~2.3 km) at Inktomi on Rhea are estimated using eq. 7b from Singer et al. (2013), assuming a loosely consolidated regolith. For those large secondaries of ~2.25 km size near the inner edge of the annular secondary zone, and estimated impact velocities of ~100 m/s (eq. 1 in Singer et al. 2013), we estimate largest fragment diameters of ~1100 m. This is similar to their estimated fragment diameters for the largest Tyre secondaries on Europa and suggests that fragmentation characteristics of ejecta may be similar on the two bodies despite differences in surface gravity and temperature and geologic histories.

DISCUSSION

Morphology of Complex Craters on Icy Moons of Saturn

Observations of complex crater morphology on Saturn's icy moons highlight the sharp rim scarps, hummocky and ridged floor materials, and extended mantling ejecta deposits of these craters (Figs. 1, 2, 9, and 13). The floor hummocks and curvilinear ridges and scarps are characteristic of craters in the ~10–300 km size range and likely reflect both uplift of floor material and collapse and slumping of rim material in an incoherent manner, given that coherent fault-bounded terraces like those observed in larger lunar craters are absent. Schenk et al. (2019) have noted that almost identical crater floor morphologies are observed in 10–40 km crater diameters on the ice-rich asteroid 1 Ceres. They attributed this to the dominance of the weaker water ice phases in Ceres' outer layers during the extremely high strain crater excavation and modification stages.

Unlike lunar craters, Cassini imaging data and derived topography show that impact melt (i.e., water) did not form in sufficient quantities to accumulate in local depressions in complex craters as large as 95 km in these icy satellites (Figs. 1, 2, 9, 15; craters > 100 km were not considered but a survey of global imaging indicates a general lack of ponded impact deposits even at larger sizes). During a hypervelocity impact, shock waves traverse the target producing a quasi-spherical region that is shocked to the point of melting. This region is typically assumed to be well approximated by a sphere of radius a few times the impactor radius (r_p) and buried at a depth ~$2 - 3 \times r_p$ (Pierazzo et al. 1997;

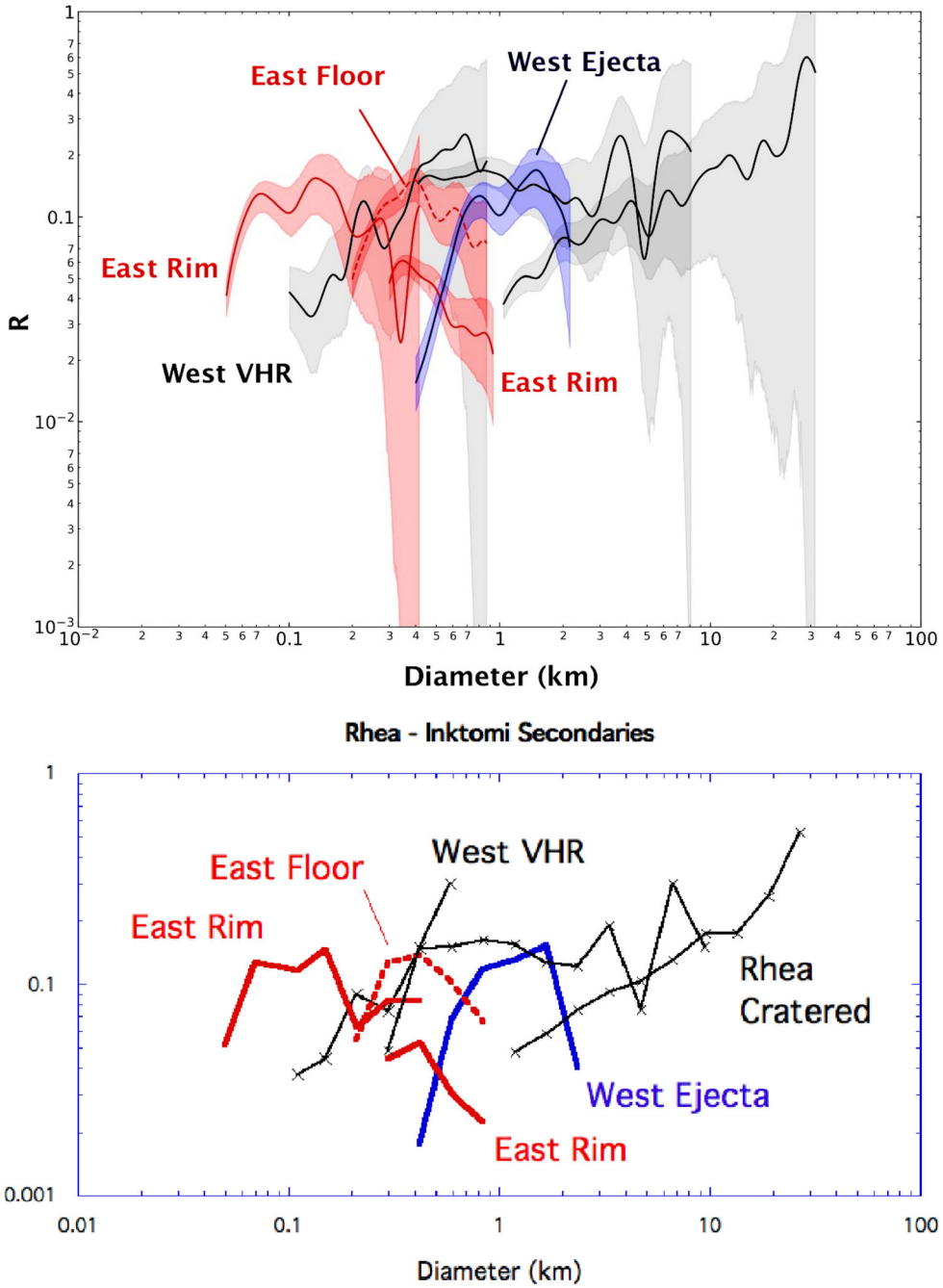

Fig. 16. Crater size–frequency distribution R-plots for secondary craters ("West Ejecta") and potential self-secondary craters ("East Rim," "East Floor") associated with Inktomi crater and cratered terrains ("West VHR" and "cratered") on Rhea. Top figure shows a kernel density estimator and bootstrap uncertainty version using techniques described in Robbins et al. (2018). These techniques reduce binning effects and better represent the error. Bottom figure shows the traditional sqrt(2) binned as described in Crater Analysis Techniques Working Group (1979) for comparison. See Figs. S10–S12 for counting areas, and Table 1 for imaging resolutions of each site (the resolution of the West Ejecta site is ~45 m, well below the lowest data plotted indicating the roll-off at small diameters is real).

Barr and Citron 2011; Melosh 1989), with subsequent redistribution across the floor and ejecta during excavation and modification. Scaling relationships developed using the hydrocode CTH (Barr and Citron 2011) suggest that the melt volume can be modeled as a sphere of radius:

$$r_m = r_p a_\chi \left(\frac{v_i}{40}\right)^{b_\chi},$$

where v_i is impact velocity in km s^{-1}, and a_χ and b_χ are material-dependent scaling parameters. Here, we compare the expected melt pool size on Rhea to that on the Moon to a first order and then specifically for Inktomi crater and a similarly sized crater on the Moon. The typical impact velocity on Rhea is 16 km s^{-1} (Zahnle et al. 2003), while on the Moon, it is 20 km s^{-1} (Le Feuvre and Wieczorek 2011). For simplicity, we assume the projectile radii are the same, and only consider the differences in v_i and the material-dependent scaling parameters. The expected melt pool size on Rhea when compared to the Moon would then be some two times as big, assuming $a_\chi = 6.05$ and $b_\chi = 0.622$ for an ice-on-ice impact, as expected for Rhea, and $a_\chi = 2.90$ and $b_\chi = 0.693$ for a dunite-on-dunite impact, which is representative of an asteroidal impact on the Moon (Barr and Citron 2011).

To precise this calculation for Inktomi, we consider the full range of impact parameters that may have led to the formation of this $D = 47$ km diameter crater on Rhea and a similar sized crater on the Moon. Indeed, a range of impact velocities, impactor radii, and impact angles (θ) can lead to the same final crater diameter. This relationship is typically given via a Pi-group scaling law. Here, we use the formulation from Ivanov and Artemieva (2002), which follows:

$$D = 2\left(\frac{\rho_p}{\rho_t}\right)^{\frac{1}{3}} r_p^{0.78} (v_i \sin\theta)^{0.43} g^{-0.22}$$

where ρ is the density of the projectile (p) and target (t), respectively, and g is the target's gravity. After solving for r_p, we then used Monte Carlo methods to identify the impact parameters that led to the formation of a $D = 47$ km diameter crater. Over 1000 instances, we randomly selected an impact velocity, assuming it follows a Raleigh distribution about its mean value, and an impact angle, assuming it follows a distribution of the form $\sin 2\theta$ such that $\theta = 45°$ is the most common value (Barr and Canup 2010; Rivera-Valentín and Barr 2014a, 2014b; Rivera-Valentin et al. 2014), and calculated the resulting projectile radius and impact melt pool radius. The simulation was conducted for Rhea and the Moon; the average over the ensemble with the standard deviation was then used.

We find that a crater the size of Inktomi on Rhea was likely formed by a projectile of radius $r_p = 2.0 \pm 1.5$ km and on the Moon by $r_p = 3.0 \pm 2.1$ km. The impact would result in a quasi-spherical melt pool on Rhea with a radius of $r_m = 5.7 \pm 2.2$ km and on the Moon a radius of $r_m = 4.3 \pm 1.4$ km. Thus, a $D = 47$ km diameter crater on Rhea would produce an impact melt pool with a sphere of radius 1.3 ± 0.7 times the size of a similar lunar crater's impact melt pool. Within the likely uncertainty of the impact parameters that led to the formation of an Inktomi-sized crater, our results indicate that produced melt pool volumes on Rhea could be lower, similar, or greater than comparable sized lunar craters.

Extensive mantling ejecta and floor deposits clearly formed at Inktomi and the other craters in this study (Figs. 1, 2, and 8), but the complete lack of evidence for ponded melt deposits on these satellites seems to be in contradiction to our calculations. This is not to say that there is no melt finely dispersed throughout the ejected or floor deposits, but that it did not accumulate on the surface in local depressions in any quantities like those observed on the Moon or other large bodies. The question then becomes one of where the melt went or whether it formed at all. Missing melt could have drained into the subsurface via impact-induced fractures, but this process is likely to be inefficient due to freezing of melt in debris-choked fractures in the floor, thus clogging them as at terrestrial craters (e.g., Pilles et al. [2018] and references therein). Some residual "stranded" surface melt deposits would be expected in any natural experiment due to subsurface rapid freezing, especially in the ejecta areas (which are much less fractured and retain little impact heat). It also seems unlikely that such large quantities of melt would have frozen in place draped on the steep slopes as they were deposited.

It is possible that true impact melts do not form in large quantities on these satellites. Porosity is likely to be broadly comparable in the impact-generated regoliths of the Moon and Rhea and thus unlikely to factor extensively into differences in melt production. The formation of pancake ejecta on icy bodies (e.g., Fig. 1) could be interpreted as evidence of enhanced melt in the ejecta, but the prominent outer scarp suggests much higher viscosities than liquid water with no evidence for outflow on any of these deposits. More likely, the lack of large quantities of impact melt is real and places important constraints on heat deposition into the target during impact on these bodies. Schenk et al. (2019) also note that the same "ponded" flat-lying floor deposits so conspicuously absent in the Saturn system are common in craters 40–100 km across on Ceres, which they attribute to melting of ice to produced now-solidified impact melt (i.e., water-rich muds) despite lower impact velocities of only ~5 km s^{-1}. The higher surface temperatures and higher proportion of non-ice materials in the crust (perhaps up to 40%) of Ceres (Ermakov et al. 2017) may lead to enhanced impact melt production there but further investigation is needed.

Formation of Secondaries on Mid-Sized Icy Bodies

Bierhaus et al. (2012) discuss the formation of secondary craters in the Saturn system from a theoretical perspective. The high-resolution observations of Inktomi provide the best-resolved sample of secondary craters in the Saturn system (Fig. 13). Examples are limited by the infrequent number of pristine large craters and high-resolution observations, but secondary craters can also be identified on the other satellites at the large fresh complex craters Sagaris, Telemachus, and Yu-ti (Figs. 1, 2; Figs. S1 and S2), all in the 45–95 km diameter range. A significant population of <15 km secondary craters is also suspected on Tethys as a result of the 400 km Odysseus impact (e.g., Schenk et al. 2018a), but requires further study. With the exception of putative secondaries from Odysseus and other large basins, these secondaries are in the <3 km size range and likely contribute significantly only to those populations as there are few primary craters >100 km across.

Modeling of ejecta and secondary crater formation on Rhea and smaller satellites predict that secondaries can form on Rhea, Dione, and Tethys (Bierhaus et al. 2012), a prediction confirmed here for craters in the 45–95 km size range (Figs. 1, 2; Figs. S1 and S2). Thus, at least hundreds of secondaries (and perhaps sesquinaries) per primary can contribute to and contaminate small (<3 km) crater statistics on these bodies. The apparent lack of observed secondaries on Iapetus and Mimas may also be consistent with these predictions (Bierhaus et al. 2012), subject to caveats regarding gaps in coverage and variability in imaging resolution on these two bodies. We note that while secondary craters were observed over a range of diameters on Ganymede (Schenk and Ridolfi 2002; Hoogenboom et al. 2015), we only have documentation of secondaries for primary craters on mid-sized icy bodies in the ~45 to 90 km size range, and we do not constrain the smallest diameter for which secondary craters can form on these moons as predicted by Bierhaus et al. (2012).

The secondary craters observed on these moons all form at distances of roughly one crater diameter from the rim and greater, as they do on the Moon, Ganymede, and Mars (Hoogenboom et al. 2015) and Europa (Schenk and Turtle 2009; Robbins and Hynek 2011; Singer et al. 2013). This range also corresponds approximately with the outer limits of the continuous ejecta deposit, suggesting that this transition occurs in a scale-independent manner (e.g., Schenk and Ridolfi 2002), as predicted by Housen et al. (1983), and does not expand or contract laterally with surface gravity or composition. Alvarellos et al. (2005) conclude that the Housen et al. (1983) and Housen and Holsapple (2011) models for scaling of ejecta velocity should apply if the target surfaces are loosely consolidated, as in a regolith, and the results shown here support this interpretation.

Formation of Self-Secondaries at Inktomi and on Mid-Sized Icy Bodies

Several possible origins can be considered for the unusual eastern Inktomi floor/rim crater field (Figs. 14 and 15) related to either endogenic/explosion pitting or impact scenarios. Densely spaced pits are found on the bottoms of crater floors and within isolated "ponded" units in low-lying areas in the ejecta of some fresh craters on Vesta (Denevi et al. 2012), and in most well-preserved Martian craters (e.g., Tornabene et al. 2012). These pits have been attributed to volatile release within spatially limited impact melt deposits on the floor and ejecta of pristine craters. In contrast, the eastern floor craters at Inktomi are not restricted to lows or to any geologic deposit or unit but rather cross all terrains, slopes, and elevations indiscriminately (Figs. 14 and 15). Furthermore, the pits on Mars and Vesta display irregular rim morphologies and do not resemble ordinary impact craters, as do these. We thus conclude that the Inktomi floor/rim craters are not volatile release or explosion pits, but are related to impact in some way.

Alternative impact mechanisms for creating the eastern floor/ejecta craters of Inktomi are limited. A swarm of small particles could trail an impacting comet but may be more likely to produce a chain of some sort along the projected track of the comet, not an elliptical cluster of intact craters on top the resulting primary crater during its excavation. Without explicit modeling, we can only assume that any Inktomi ejecta debris that leaves Rhea's gravitational influence (i.e., sesquinary [e.g., Alvarellos et al. 2005]) would be quickly dispersed into a debris "cloud" much larger than the observed 20×50 km wide crater cluster on eastern Inktomi, due to the complex gravitational regime involving Saturn, Rhea, and Titan. Furthermore, it would seem highly unlikely for debris to have traveled outside the gravitation control of Rhea only to reimpact exactly on its source rather than somewhere else on Rhea (considering that the area of the crater field on the floor is only ~1/1000 the projected area of Rhea's disk).

Given the extreme youth of Inktomi and the lack of evidence for an endogenic origin of these small floor craters, a form of secondary cratering is most likely. Morphologies and distributions of the craters on the eastern floor of Inktomi crater (Figs. 14 and 15) are consistent with origins as secondary craters. A combined high-resolution photoclinometry–stereogrammetry DEM

of eastern floor/rim site (Fig. 15) suggests that craters here may have shallow depth/diameter values close to 0.1 (Fig. S13 in supporting information), rather than the canonical 0.2 for fresh primaries of similar size. Although these depths may be uncertain by up to 25%, they suggest that crater shapes here may be shallow in the same way usually attributed to lower velocity secondary craters. These craters also have apparent brightness similar to the Inktomi floor and ejecta deposits they formed on, suggesting they formed essentially contemporaneously with it, as would secondary craters.

A suitable source crater other than Inktomi itself is missing. The largest of the craters in the eastern Inktomi floor crater field is ~0.9 km in diameter (Figs. 13 and 16). By the scaling rules established for lunar and Europan craters (Allen 1979; Singer at al. 2013), which require that the largest secondaries have diameters of 0.04–0.05 as the primary diameter, this would require a source primary crater at least 25 km across. Inktomi is by far the largest and brightest of ~26 rayed craters identified on Rhea (Schenk and Murphy 2011). The next largest of Rhea's rayed craters is only 7 km across (updated from Schenk and Murphy 2011) and at less than one-fifth of the diameter of Inktomi incapable of producing any secondary craters larger than ~350 m, and at ~1700 km distance incapable of delivering any significant quantity to the Inktomi site. The only plausible source of large numbers of clustered craters of these sizes is Inktomi itself, and we conclude that these eastern floor/ejecta craters formed by fallback of secondary ejecta fragments on near vertical trajectories to land within and on the rim of the source crater, a process referred as "self-secondary" cratering.

The dense fields of small craters observed on the Inktomi floor and ejecta (Figs. 1, 2; Figs. S1 and S2) are not normally observed on the floors of the most recently formed large craters on other bodies. Mapping of small craters shows factors of four or more difference in crater densities within ejecta units proximal to recent large lunar craters (Plescia and Robinson 2015; Zanetti et al. 2017), though lunar studies do not address floor craters in detail. These craters display characteristic clustering and quasi-herringbone ejecta patterns of secondaries but are not as densely spaced as the examples at Inktomi. Self-secondaries are also documented at Occator on Ceres (Neesemann et al. 2019). Boyce and Mouginis-Mark (2015) report higher densities of small craters on part of the outer slopes immediately adjacent to the rim scarp of very young 28 km Tooting crater on Mars (Fig. 17) that may also be self-secondary craters not unlike the abundant small craters in the eastern ejecta of Inktomi (Fig. 14), though not as widely dispersed.

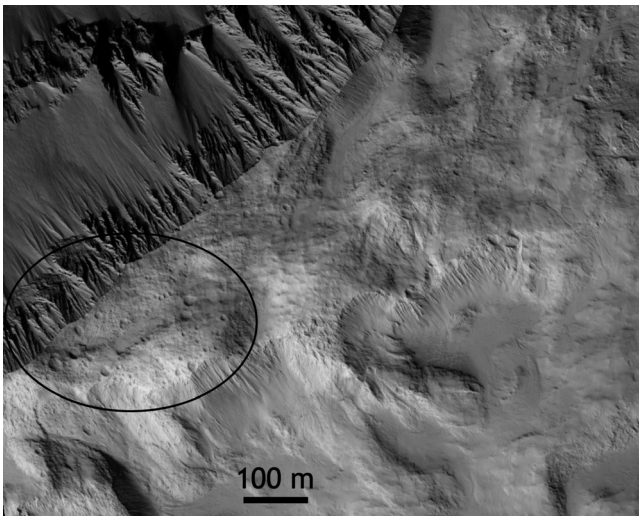

Fig. 17. High-resolution view of southeastern rim flank of Tooting crater, Mars, showing cluster of small probable self-secondary craters (oval; e.g., Boyce and Mouginis-Mark 2015). Note the absence of similar craters to the upper right (and elsewhere on the rim). Crater center is to upper left. HiRISE image at pixel scales of <1 m.

By their irregular and inconsistent distributions, self-secondary craters defy the standard, well-ordered scenario for secondary crater formation in annular patterns around primary craters. As such they are not formed as part of the classical ejecta process but require a more poorly understood and probably unpredictable or stochastic mechanism not included in most cratering models or experiments. Proposed explanations for self-secondaries include early-phase near-vertical launch of spalled impact debris (cf. Plescia and Robinson 2015; Xiao 2018) that reimpacts the recently formed primary crater, or rotation of the impact site under the expanding ejecta curtain on fast-rotating bodies (e.g., Schmedemann et al. 2017). Surfaces of rapid rotators such as Vesta and Ceres could outrun the expanding ~ 45° curtain of ejecta fragments (Schmedemann et al. 2017) and these models successfully predict the location of clusters of self-secondaries across the floor and ejecta of the very recent 92 km wide Occator crater on Ceres (Neesemann et al. 2019). Ejecta modeling tools that predict fragment dispersal on rotating spheroidal bodies (Xiao et al. 2016; Schmedemann et al. 2017; Neesemann et al. 2019) can be valuable in predicting where ejecta fragments will fall on such bodies, but do not yet take into account irregularities in initial local target properties (e.g., topographic, structural, and lithologic variability) and the effects those will have on ejecta dispersal. Although likely due to planetary rotation on small bodies such as Vesta and Ceres (Schmedemann et al. 2017), the fact that both the Moon and Mercury are

very slow rotators also demonstrates that planetary rotation cannot explain all occurrences of self-secondary cratering. Rhea is also a slow rotator at ~4.5 days, too slow to allow for rotation of the primary crater under a normally expanding ejecta curtain, and not-quite-vertical spallation is the more likely explanation on such bodies.

We suggest that the rugged pre-existing topography at Inktomi (Figs. 9 and 10) or elsewhere modulates or disrupts the normally symmetric cratering excavation and fragment ejection process to produce near-vertical ejecta. The oval field of craters is on the eastern quadrant of Inktomi floor, along the oblique east–west impact direction inferred from the asymmetric ray patterns (Fig. 4). This, and irregularities in the excavation flow field induced by large localized variations in pre-existing surface topography on Rhea, which can vary vertically by more than a kilometer over distances of <5 km (Fig. 13), may have induced localized near-vertical spallation and ejection of debris. Whether the formation of self-secondaries is linked to oblique impact, irregular surface topography, or both, is unclear from this single example but may be demonstrated by mapping on other solar system solid bodies and numerical simulations of impact physics under such conditions. Impact experiments and models are usually performed in targets with little or no relief. Rhea is essentially saturated in cratering with local relief of several kilometers over short distances. The influence of such prominent relief in early stage impact crater formation and ejection, including the possible formation of near-vertical fragment ejection, requires further investigation.

Another possibility is that fragmented or rubbly material is detached and lofted into space when the central peak reaches its highest elevation during the floor rebound process (e.g., Melosh 1989). This process would also by nature be stochastic and dependent on local impact conditions and material properties. Numerical simulations of processes at the radial centers of impact craters are notoriously difficult due to edge ambiguities, but more advanced modeling techniques may be able to distinguish between these hypotheses. However, we observe no direct evidence of missing mass on the crest of central peaks on these craters.

The circularity of many of the craters in the Inktomi floor/rim field is broadly consistent with relatively higher angles of impact. This is unlikely to be vertically launched ejecta as even the slow rotation of Rhea (~4.5 Earth days) will carry the impact site out of range of any vertically launch debris within <1 h; near-vertical is all that is required. Any returning ejecta must have been launched at <560 m s^{-1} to avoid escape, implying a maximum travel time from ejection to return of no more than ~70 min. This requires Inktomi to have undergone the collapse process and formed the observed floor mounds and central peak within this time period.

Several small volumetrically insignificant postimpact debris slides on the northwestern rim scarp appear to have overrun some of these floor craters (Fig. 10; Fig. S6), suggesting minor rim modification occurred after the formation of the craters (and could have been partially triggered by these small craters). Otherwise, the vast majority of the small craters on Inktomi's floor are undisturbed and formed on a crater floor that had mostly been emplaced and solidified (Fig. 9). The stereo images of all four of the large complex craters studied here (Figs. 1, 2, 9; Figs. S1 and S2) demonstrate that essentially no significant volumes of locally ponded impact melt formed on either the floor or ejecta, permitting self-secondaries to form on a solidified though disrupted surface. These observations constrain the projectiles to have traveled far enough upward to have allowed the crater excavation and modification processes to have gone to completion before reimpacting the crater surface (melt not being significant). This implies that the rim scarp, floor mounds, and ridges and the central peak, followed by secondary craters, all formed very quickly (occasional postimpact rim wall debris slides notwithstanding). Further constraining the sequence is the apparent overriding of these floor craters by a few small late-stage landslides on the northeast rim (Fig. 10).

The origin of the circa 50% smaller dominant sizes of craters in the eastern floor/ejecta crater field compared to the classical secondaries to the north, west, and south is also unclear. Self-secondaries are likely to be ejected from and strike the surface nearly vertically (or at least more so than normal secondaries) and at something approaching the escape velocity of the target body. They therefore impact at higher velocities and angles than do more distance secondaries, which generally hit the surface at angles around 45°. This would likely increase cratering efficiency and require that the fragments be smaller than for normal secondaries. We conjecture that the fragments producing self-secondaries in the eastern floor/ejecta crater field at Inktomi were probably more intensely fractured by the spallation and launching process and resulted in smaller projectiles.

Floor craters have not yet been identified at any of the other fresh icy satellite craters described in this report. Those craters were observed at pixel scales of 200–250 m or worse (Figs. 1 and 2) and any self-secondaries on the floors of these craters, which may be half the size of regular secondaries based on the Inktomi findings, might not be resolvable. Thus, it remains unknown whether similar floor craters occur at any other craters in the Saturn system.

Studies of self-secondary craters on the Moon, Mercury (Xiao et al. 2016; Zanetti et al. 2017), possibly Mars (Boyce and Mouginis-Mark 2015), and now icy satellites (this report) point to a potentially significant contribution of self-secondaries to the populations of small craters on recently formed larger craters. These have the potential to confuse crater counts designed to derive ages of young craters (e.g., Hiesinger et al. 2012; Zanetti et al. 2017). We note that nearly all of these craters on Inktomi's floor are undetectable in images acquired at pixel scales larger than 100 m, due to their smaller sizes, and efforts to identify and map such craters on other targets will require adequate resolution. In some cases, only the largest of these fallback craters might be recognizable, leading to the conclusion that only a few postimpact primaries formed on the surface and further confusing their identity.

CONCLUSIONS

Inktomi and other observations (Figs. 2, 3, and 14) reveal details on the cratering process on mid-sized icy bodies, including the formation of ridged floor deposits and the lack of recognizable impact melt deposits, an important consideration for impact modeling. They also reveal mantling ejecta units and classical secondary craters, and that these scale similar to those on other planetary bodies, at least in the 45–95 km crater range.

Distinct from classical secondary craters, the formation of hundreds of small craters <1 km across on the fresh bright rayed crater Inktomi (Figs. 14 and 15) represents an extreme example of self-secondary cratering, in which ejecta fragments fall back onto the primary itself. Studies of lunar, mercurian, cerean, and now rhean craters confirm that this planetary cratering process is widespread but also relatively uncommon, highly variable in expression, and not well accounted for in most impact models. Self-secondaries can be densely concentrated as at Inktomi or more broadly and unevenly dispersed across the floor or continuous ejecta blanket as in the mercurian and lunar examples and hence more difficult to distinguish from background primary cratering, especially as later small primary craters accumulate. The tightly clustered nature of the Inktomi floor and rim craters indicates either a cloud of fragments was ejected or a smaller number of larger fragments broke apart during flight. At Inktomi, self-secondaries produce craters roughly a factor of two smaller than regular secondary craters (Fig. 16), but that because of likely near vertical impact conditions, the fragments that produced them might have an even smaller size ratio than those for regular secondaries.

Minimization of the effects of possible non-uniformly distributed self-secondary contamination in cratering statistics requires the use of the entire crater floor and ejecta as counting areas to reduce the number of self-secondaries included, and quotation of ages as maximum ages due to the potential presence of non-primary cratering. Efforts to determine the ages of larger craters should consider potential self-secondary contamination through detailed examination of the spatial density variability across the entire crater floor and ejecta deposit. The added complexity of unpredictable and stochastic self-secondaries to recent crater units only increases the urgency of devising improved methods for dating the formation of surfaces in the outer solar system and improving our understanding of secondary cratering generally.

Acknowledgments—We thank Tilmann Denk for recognizing the importance of Inktomi and planning these observations and the Cassini Data Analysis and Participating Scientist programs for supporting this work. We also thank B. Bierhaus and S. Robbins for highly detailed and insightful reviews.

Editorial Handling—Dr. Gordon Osinski

REFERENCES

Allen C. C. 1979. Large lunar secondary craters: Size-range relationships. *Geophysical Research Letters* 6:51–54.

Alvarellos J., Zahnle K., Dobrovolskis A., and Hamill P. 2005. Fates of satellite ejecta in the Saturn system. *Icarus* 178:104–123.

Barr A. C. and Canup R. M. 2010. Origin of the Ganymede-Callisto dichotomy by impacts during the late heavy bombardment. *Nature Geoscience* 3:164–167.

Barr A. C. and Citron R. I. 2011. Scaling of melt production in hypervelocity impacts from high-resolution numerical simulations. *Icarus* 211:913–916.

Bierhaus E. B., Dones L., Alvarellos J. L., and Zahnle K. 2012. The role of ejecta in the small crater populations on the mid-sized Saturnian satellites. *Icarus* 218:602–621.

Bierhaus E., McEwen A., Robbins S., Singer K., Dones L., Kirchoff M., and Williams J.-P. 2018. Secondary craters and ejecta across the solar system: Populations and effects on impact-crater-based chronologies. *Meteoritics & Planetary Science* 53:638–671.

Boyce J. and Mouginis-Mark P. 2015. Anomalous areas of high crater density on the rim of the Martian crater Tooting. In Abstracts of the workshop on issues in crater studies and the dating of planetary surfaces, Laurel, Maryland, May 19–22.

Chapman C., Baker D., Barnouin O., Fassett C., Marchi S., Merline W., Ostrach I., Prockter I., and Strom R. 2018. Impact cratering on Mercury. In *Mercury: The view after MESSENGER*, edited by Solomon S. C., Nittler L. R., and Anderson B. J. Cambridge: Cambridge University Press. pp. 217–248.

Denevi B., Blewett D. T., Buczkowski D. L., Capaccioni F., Capria M. T., De Sanctis M. C., Garry W. B., Gaskell R.

W., Le Corre L., Li J.-Y., Marchi S., McCoy T. J., Nathues A., O'Brien D. P., Petro N. E., Pieters C. M., Preusker F., Raymond C. A., Reddy V., Russell C. T., Schenk P., Scully J. E. C., Sunshine J. M., Tosi F., Williams D. A., and Wyrick D. 2012. Pitted terrain on Vesta and implications for the presence of volatiles. *Science* 338:246–249.

Ermakov A. I., Fu R., Castillo-Rogez J. C., Raymond C. A., Park R. S., Preusker F., Russell C. T., Smith D. E., and Zuber M. T. 2017. Constraints on Ceres' internal structure and evolution from its shape and gravity measured by the Dawn spacecraft. *Journal of Geophysical Research: Planets* 123:2267–2303.

Gault D. E., Guest J. E., Murray J. B., Dzurisin D., and Malin M. C. 1975. Some comparisons of impact craters on Mercury and the Moon. *Journal of Geophysical Research* 80:2444–2460.

Hiesinger H., van der Bogert C., Paskert J., Funcke L., Giacomini L., Ostrach L., and Robinson M. 2012. How old are young lunar craters? *Journal of Geophysical Research* 117. https://doi.org/10.1029/2011JE03935

Hirata N. and Miyamoto H. 2016. Rayed craters on Dione: Implication for the dominant surface alteration process. *Icarus* 274:116–121.

Hoogenboom T., Johnson K., and Schenk P. 2015. Contribution of secondary craters on the icy satellites: Results from Ganymede and Rhea (abstract #2530). 46th Lunar and Planetary Science Conference. CD-ROM.

Housen K. and Holsapple K. 2011. Ejecta from impact craters. *Icarus* 211:856–875.

Housen K., Schmidt R., and Holsapple K. 1983. Crater ejecta scaling laws: Fundamental forms based on dimensional analysis. *Journal of Geophysical Research* 88:2485–2499.

Ivanov B. A. and Artemieva N. A. 2002. Numerical modeling of the formation of large impact craters. *Geological Society of America Special Paper* 356:619–630.

Kirchoff M. R. and Schenk P. M. 2010. Impact cratering records of the mid-sized, icy Saturnian satellites. *Icarus* 206:485–497. https://doi.org/10.1016/j.icarus.2009.12.007

Kirchoff M. K., Bierhaus E. B., Dones L., Robbins S. J., Singer K. N., Wagner R. J., and Zahnle K. J. 2018. Cratering histories in the saturnian system. In *Enceladus and the icy moons of Saturn*, edited by Schenk P., Clark R. N., Howett C. J. A., Verbiscer A. J., and Waite J. H. Tucson, Arizona: University of Arizona Press. pp. 267–284.

Kruger T., van der Bogert C. and Hiesinger H. 2016. Geomorphological mapping of the lunar crater Tycho and its impact melt deposits. *Icarus* 273:164–181.

Le Feuvre M. and Wieczorek M. A. 2011. Nonuniform cratering of the Moon and a revised crater chronology of the inner solar system. *Icarus* 214:1–20.

McEwen A. and Bierhaus E. 2006. The importance of secondary cratering to age constraints on planetary surfaces. *Annual Review of Earth and Planetary Sciences* 34:535–567.

McEwen A. S., Preblich B. S., Turtle E. P., Artemieva N. A., Golombek M. P., Hurst M., Kirk R. L., Burr D. M., and Christensen P. R. 2006. The rayed crater Zunil and interpretations of small impact craters on Mars. *Icarus* 176:351–81.

Melosh H. J. 1989. *Impact cratering: A geologic process*. New York: Oxford University.

Mouginis-Mark P. J. and Boyce J. M. 2012. Tooting crater: Geology and geomorphology of the archetype large, fresh, impact crater on Mars. *Chemie der Erde* 72:1–23. https://doi.org/10.1016/j.chemer.2011.12.001

Neesemann A., van Gasselt S., Schmedemann N., Marchi S., Walter S., Preusker F., Michael G., Kneissl T., Hiesinger H., Jaumann R., Roatsch T., Raymond C., and Russell C. 2019. The various ages of Occator crater, Ceres: Results of a comprehensive synthesis approach. *Icarus* 320:60–82. https://doi.org/10.1016/j.icarus.2018.09.006

Pilles A., Osinski G., Grieve R., and Tornabene L. 2018. A review of impact melt and breccia dykes in terrestrial impact structures (abstract #1994). 49th Lunar and Planetary Science Conference. CD-ROM.

Pierazzo E., Vickery A. M., and Melosh H. J. 1997. A reevaluation of impact melt production. *Icarus* 127:408–423.

Plescia J. and Robinson M. 2015. Lunar self-secondary cratering: Implications for cratering and chronology (abstract #2535). 46th Lunar and Planetary Science Conference. CD-ROM.

Plescia J. B. and Robinson M. S. 2019. Giordano Bruno: Small crater populations—Implications for self-secondary cratering. *Icarus* 321:974–93.

Rivera-Valentin E. G., and Barr A. C. 2014a. Estimating the size of late veneer impactors from impact-induced mixing on Mercury. *Astrophysical Journal Letters* 782:L8.

Rivera-Valentin E. G. and Barr A. C. 2014b. Impact-induced compositional variations on Mercury. *Earth and Planetary Science Letters* 391:234–242.

Rivera-Valentin E. G., Barr A. C., Lopez Garcia E. J., Kirchoff M. R., and Schenk P. M. 2014. Constraints on planetesimal disk mass from the cratering record and equatorial ridge on Iapetus. *The Astrophysical Journal* 792:127.

Robbins S. J. and Hynek B. M. 2011. Secondary crater fields from 24 large primary craters on Mars: Insights into nearby secondary crater production. *Journal of Geophysical Research* 116:E10003. https://doi.org/10.1029/2011JE003820.

Robbins S., Runyon K., Singer K. N., Bray V. J., Beyer R. A., Schenk P., McKinnon W. B., Grundy W. M., Nimmo F., Moore J. M., Spencer J. R., White O. L., Binzel R. P., Buie M. W., Buratti B. J., Cheng A. F., Linscott I. R., Reitsema H. J., Reuter D. C., Showalter M. R., Tyler G. L., Young L. A., Olkin C. B., Ennico K. S., Weaver H. A., and Stern S. A. 2018. Investigation of Charon's craters with abrupt terminus ejecta, Comparisons with other bodies and formation implications. *Journal of Geophysical Research* 123:20–36. https://doi.org/10.1002/2017JE005287.

Schenk P. and Murphy S. 2011. The rayed craters of Saturn's icy satellites (including Iapetus): Current impactor populations and origins (abstract #2098). 42nd Lunar and Planetary Science Conference. CD-ROM.

Schenk P. and Ridolfi F. 2002. Morphology and scaling of ejecta deposits on icy satellites. *Geophysical Research Letters* 29. https://doi.org/10.1029/2001GRL013512

Schenk P. and Turtle E. 2009. Europa's impact craters: Probes of the interior. In *Europa*, edited by Pappalardo R. T., McKinnon W. B., and Khurana K. Tucson, Arizona: University of Arizona Press. pp. 181–198.

Schenk P., Chapman C., Zahnle K., and Moore J. 2004. Ages and interiors, the cratering record of the Galilean

Satellites. In *Jupiter*, edited by Bagenal F. Cambridge: Cambridge Press. pp. 427–456.
Schenk P., Hamilton D., Johnson R., McKinnon W., Schmidt J., and Showalter M. 2011. Plasma, plumes, and rings: Global color patterns on Saturn's midsize icy satellites. *Icarus* 211:740–757.
Schenk P., White O., Moore J., and Byrne P., et al. 2018a. Geology of Saturn's other icy moons. In *Enceladus and the icy moons of Saturn*, edited by Schenk P., Clark R. N., Howett C. J. A., Verbiscer A. J., and Waite J. H. Tucson, Arizona: University of Arizona Press. pp. 237–266.
Schenk P., Beyer R. A., McKinnon W. B., Moore J. M., Spencer J. R., White O. L., Singer K., Nimmo F., Thomason C., Lauer T. R., Robbins S., Umurhan O. M., Grundy W. M., Stern A., Weaver H. A., Young L. A., Ennico Smith K., Olkin C., and the New Horizons Geology and Geophysics Investigation Team. 2018b. Basin, fractures and volcanoes: Global cartography and topography of Pluto from new horizons. *Icarus* 314:400–433.
Schenk P., Sizemore H., Schmidt B., Castillo-Rogez J., De Sanctis M., Bowling T., Scully J., Buczkowski D., Quick L., Preusker F., Park R., Raymond C., and Russell C. 2019. The central pit and dome at Cerealia Facula bright deposit and floor deposits in Occator crater, Ceres: Morphology, comparisons and formation. *Icarus* 320:159–187.
Schmedemann N., Neesemann A., Schulzeck F., Krohn K., von der Gathen I., Otto K. A., Jaumann R., Wagner R., Michael G., Raymond C. A., and Russell C. T. 2017. How the distribution of impact ejecta may explain surface features on Ceres and Saturnian satellites. European Planetary Science Congress 2017. id. EPSC2017-119.
Shoemaker E. M. 1967. Interpretation of lunar craters. In *Physics and astronomy of the moon*, edited by Kopal Z. New York: Academic Press. pp. 283–359.
Shoemaker E., Batson R., Holt H., Morris E., Rennilson J., and Whitaker E. 1968. Television observations from surveyor VII, in surveyor VII mission report, part II, science results. *National Aeronautics and Space Administration Technical Reports* 32–126A:9–76.
Shoemaker E. M., Morris E., and Batson R. 1969. Television observations from Surveyor. Surveyor Program Results, SP-184, NASA, pp. 19–128.
Singer K., McKinnon W., and Nowicki L. 2013. Secondary craters from large impacts on Europa and Ganymede: Ejecta size–velocity distributions on icy worlds, and the scaling of ejected blocks. *Icarus* 226:865–884.
Stephan K., Jaumann R., Wagner R., Clark R. N., Cruikshank D. P., Giese B., Hibbitts C. A., Roatsch T., Matz K.-D., Brown R. H., Filacchione G., Cappacioni F., Scholten F., Buratti B. J., Hansen G. B., Nicholson P. D., Baines K. H., Nelson R. M., and Matson D. L. 2012. The Saturnian satellite Rhea as seen by Cassini VIMS. *Planetary and Space Science* 61:142–160.
Tornabene L., Osinski G. R., McEwen A. S., Boyce J. M., Bray V. J., Caudill C. M., Grant J. A., Hamilton C. W., Mattson S., and Mouginis-Mark P. 2012. Widespread crater-related pitted materials on Mars: Further evidence for the role of target volatiles during the impact process. *Icarus* 220:348–368.
Wagner R. J., Neukum G., Giese B., Roatsch T., Denk T., Wolf U., and Porco C. C. 2008. Geology of Saturn's satellite Rhea on the basis of the high-resolution images from the targeted flyby 049 on August 30 2007 (abstract #1930). 39th Lunar and Planetary Science Conference. CD-ROM.
White O. L., Schenk P. M., and Dombard A. J. 2013. Impact basin relaxation on Rhea and Iapetus and relation to past heat flow. *Icarus* 223:699–709.
White O. L., Schenk P. M., Bellagamba A. W., Grimm A. M., Dombard A. J., and Bray V. J. 2017. Impact crater relaxation on Dione and Tethys and relation to past heat flow. *Icarus* 288:37–52.
Williams J.-P., Van Derbogert C., Pathare A., Michael G., Kirchoff M., and Hiesinger H. 2018. Dating very young planetary surfaces from crater statistics: A review of issues and challenges. *Meteoritics & Planetary Science* 53:554–582.
Xiao Z. 2018. On the importance of self-secondaries. *Geoscience Letters* 5:17. https://doi.org/10.1186/s40562-018-0116-9
Xiao Z., Prieur N., and Werner S. 2016. The self-secondary crater population of the Hokusai crater on Mercury. *Geophysical Research Letters* 43:7424–7432.
Zahnle K., Schenk P., Levison H., and Dones L. 2003. Cratering rates in the outer solar system. *Icarus* 163:263–289.
Zanetti M., Stadermann A., Joliff B. L., Hiesinger H., can der Bogert C. H., and Plescia J. B. 2017. Evidence for self-secondary cratering of Copernican-age continuous ejecta deposits on the Moon. *Icarus* 298:64–77.

SUPPORTING INFORMATION

Additional supporting information may be found in the online version of this article.

Fig S1. Cassini stereo image pair of 67-km-wide Yu-ti crater on Rhea, at pixel scales of ~270 m.

Fig S2a. Cassini stereo image pair of 34-km-wide Creusa crater (49°N, 284°E) on Dione, at pixel scales of ~270 m. Data from orbits 163 and 222.

Fig S2b. Well-preserved 9-km-wide bright ray crater on Dione, showing hummocky floor deposits an ejecta deposits, including several parallel markings to the southwest (arrow) that could be deceleration dunes emplaced during ejecta deposition.

Fig S3. Cassini image of Rhea, showing 49-km-wide bright ray crater Inktomi, revealing details of the inner portions of the bright ray pattern.

Fig S4a. Cassini orbit 49 targeted 15 frame NA 3-color mosaic of bright ray crater Inktomi at 40-95 m pixel scales, Rhea, projected to orthographic map projection centered on the crater.

Fig S4b. Cassini orbit 49 targeted NA 3-color mosaic of bright ray crater Inktomi at ~210 m pixel scales, Rhea, projected to orthographic map projection centered on the crater.

Fig S4c. Orbit 162 context imaging at low Sun angle illumination and ~260 m pixel scales, highlighting topographic variations.

Fig S4d. Enlargement of Figure S4b, centered on 49-km-wide Inktomi crater and inner ejecta deposits.

Fig S5. Cassini ~4 km/pixel projected image (left) and identical projection of ~1 km/pixel Voyager mosaic (right) of bright rays east of Inktomi crater (just out of view at center left).

Fig S6. Image (left), DEM (right), and topographic profile bottom across one of several small landslide features at the base of northeast rim wall scarp of Inktomi crater.

Fig S7a. Color stereo view of western floor and rim of 49-km Inktomi crater.

Fig S7b. Stereo view of northeastern floor and rim of Inktomi crater.

Fig S8. Color ratio images of Inktomi crater, showing same area as in Fig. 4b.

Fig S9. Stereo view of western secondary crater field of Inktomi crater, showing the inner edge of the field adjacent to the continuous ejecta deposit which extends out of view to the right.

Fig S10. Counting areas and mapped craters for western secondary field, referred to as the "West Ejecta" site in the count plots.

Fig S11. Counting areas and mapped craters for the eastern crater floor (peak is at center left) referred to as the "East Floor" site. Image is ~15 km wide.

Fig S12. Counting area and mapped craters for a representative cratered terrain site on Rhea. Orbit 49 image N1567128880.118 centered at 3°N 298°E.

Fig S13. Provisional depth/diameter data for selected larger craters on the crater floor and ejecta deposits on Inktomi crater.